PROCEEDINGS OF SPIE

In-lab testing of six-level phase mask coronagraphs onto the high-contrast imaging THD2 bench

Fabien Patru, Pierre Baudoz, Raphaël Galicher, Faouzi Boussaha, Josiane Firminy, et al.

In-lab testing of six-level phase mask coronagraphs onto the high-contrast imaging THD2 bench

Fabien Patru[a], Pierre Baudoz[a], Raphaël Galicher[a], Faouzi Boussaha[b], Josiane Firminy[b], Qing Cao[c], Kai Wang[c], Lujing Xing[c], Marion Bonafous[a], Axel Potier[a]

[a] PSL Research Univ., CNRS, Sorbonne Univ., UPMC Univ. Paris 06, Univ. Paris Diderot, Sorbonne Paris Cité, Obs. Paris, LESIA, 5 place Jules Janssen, 92195 Meudon cedex, France
[b] PSL Research Univ., CNRS, Sorbonne Univ., UPMC Univ. Paris 06, Univ. Paris Diderot, Sorbonne Paris Cité, Obs. Paris, GEPI, 5 place Jules Janssen, 92195 Meudon cedex, France
[c] Department of Physics, Shanghai Univ., 99 Shangda Road, Baoshan District, Shanghai 200444, China

ABSTRACT

While radial velocity and transit techniques are efficient to probe exoplanets with short orbits, the study of long-orbit planets requires direct imaging and coronagraphic techniques. However, the coronagraph must deal with planets that are 10^4 to 10^{10} fainter than their hosting star at a fraction of arcsecond, requiring efficient coronagraphs at short angular separation. Phase masks proved to be a good solution in monochromatic or limited spectral bandwidth but expansion to broadband requires complex phase achromatization. Solutions use photonic crystals, subwavelength grating or liquid crystal polymers but their manufacturing remains complex. An easier solution is to use photolithography and reactive ion etching and to optimize the azimuthal phase distribution like achieved in the six-level phase mask (SLPM) coronagraph (Hou et al. 2014). We present here the laboratory results of two SLPM coronagraphs enabling high-contrast imaging in wide-band. The SLPM is split in six sectors with three different depths producing three levels of optical path difference and yielding to uniform phase shifts of 0, π or 2π at the specified wavelength. Using six sectors instead of four sectors enables to mitigate the chromatic effects of the SLPM compared to the FQPM (Four-Quadrant Phase Mask) while keeping the manufacturing easy. Following theoretical developments achieved by University of Shanghai and based on our previous experience to fabricate FQPM components, we have manufactured SLPM components by reactive ion etching at Paris Observatory and we have tested it onto the THD2 facility at LESIA. The THD2 bench was built to study and compare high-contrast imaging techniques in the context of exoplanet imaging. The bench allows reducing the starlight below a 10^{-8} contrast level in visible/near-infrared. In this paper, we show that the SLPM is easy to fabricate at low cost and is easy to implement with a unique focal plane mask and no need of pupil apodization. Detection of a planet can be achieved at small inner working angle down to 1 λ/D. The on-axis attenuation of the best SLPM component reaches 2×10^{-5} at $\lambda = 800$ nm and is better than 10^{-4} in intensity over a 10% spectral bandwidth. Along the diagonal transition, we show that the off-axis transmission is attenuated by less than 3% over a 10% bandwidth and will need to be calibrated. Any etching imperfections can affect the SLPM performance, by lowering the on-axis attenuation and by changing the optimal wavelength. Despite few nanometers of uncertainty for etching the depths, we show that this first component can provide a high-contrast attenuation in laboratory.

Keywords: high-contrast imaging, focal-plane wavefront sensing, coronagraphy, focal-plane phase mask, THD2 bench

1. INTRODUCTION

More than 3,500 exoplanets have been discovered by using different techniques. While radial velocity and transit techniques are efficient to probe exoplanets with short orbits, direct imaging and coronagraphic techniques enable spectral characterization of long-orbital period exoplanets in the outer part of extrasolar systems. However, the

---

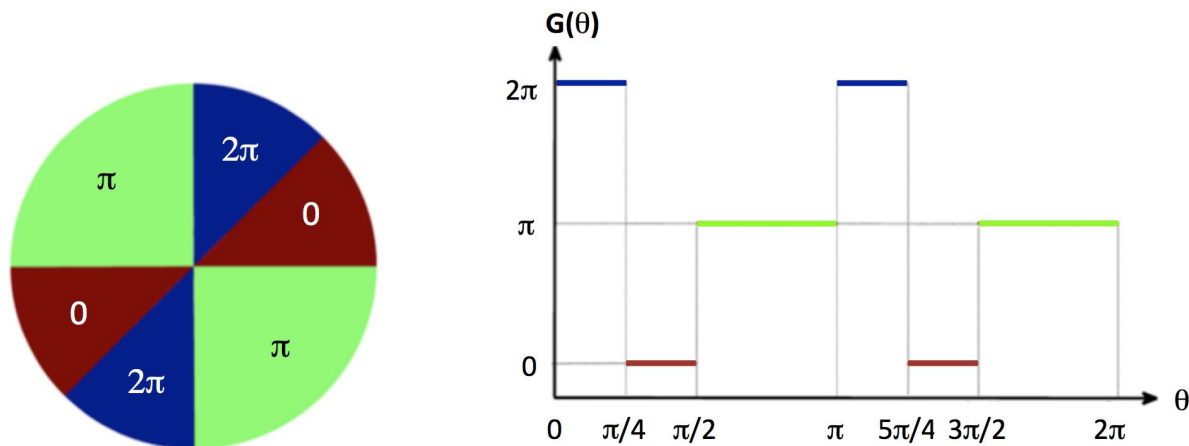Further author information: Send correspondence to fabienpatru@gmail.com

Figure 1. Left: Surface profile of the SLPM composed of six level regions. The red area is 2π-dephased with respect to the blue area. Both red and blue areas are π-dephased with respect to the green area. Right: Phase distribution in the angular direction for the designed wavelength λ_0. Figure extracted from (15) with the courtesy of Hou et al. 2014.

coronagraph must deal with planets that are 10^4 to 10^{10} fainter than their hosting star at a fraction of arcsecond, requiring efficient coronagraphs at short angular separation. Providing high-contrast images requires not only performant coronagraphs and extreme AO systems but also focal-plane wavefront-sensing techniques to avoid wavefront sensor aliasing and non-common path aberrations and to suppress the quasi-static speckles.

Among the coronagraphic concepts (1; 2), using an ideal focal-plane phase mask fully transmit the planetary flux and completely suppress the diffraction pattern of the starlight which is diffracted by the phase mask outside of the Lyot stop. A focal mask is efficient to provide direct images with a high throughput and a high starlight extinction and to detect exoplanet as close as λ/D from the central star (with D the Lyot stop diameter). The initial concept of Lyot (3) has been improved by using either pupil plane amplitude masks or focal plane phase masks, as well as hybrid phase and amplitude focal plane mask coronagraphs. Numerous phase masks have been proposed the last two decades, like for instance : the disk phase mask (DPM) (4; 5), the achromatic phase knife coronagraph (APKC) (6; 7), the dual-zone phase mask (DZPM) (8), the four-quadrant phase mask (FQPM) (9; 10; 11; 12; 13), the sinusoidal phase mask (SPM) (14), the six-level phase mask (SLPM) (15; 16), the eight-octant phase mask (EOPM) (17) as well as the optical vortex phase mask (OVC) (18; 19).

Phase masks proved to be a good solution in monochromatic or limited spectral bandwidth but expansion to broadband requires complex phase achromatization. Some achromatic designs have been proposed (20; 21; 22; 23; 24; 25; 26; 27), allowing wider bandwidths and increasing the throughput required for detecting and characterizing exoplanets. One can also propose a multistage concept (*e.g.* for the FQPM (28), the SLPM (29) or the Vortex (30)) but it remains difficult to align it and to integrate it inside an instrument. Solutions use photonic crystals, subwavelength grating or liquid crystal polymers (31) but they need a large number of manufacturing steps which can rapidly increase the fabrication defects of the component.

An easier solution of achromatization is to use well-controlled fabrication processes like photolithography and reactive ion etching and to optimize the azimuthal phase distribution like achieved in the the SLPM (15). Following theoretical developments achieved by University of Shanghai (15; 29) and based on our previous experience to fabricate FQPM components (32), we have manufactured SLPM components by reactive ion etching at GEPI and we have tested it onto the THD2 bench at LESIA in Paris Observatory (16). We present in this paper the design (Sect. 2.1), manufacturing (Sect. 2.2), control (Sect. 2.3) and testing (Sect. **??**) of two SLPM components. We compare the coronagraphic performance (Sect. 4) obtained in laboratory with numerical simulations (Sect. 5) properly fitting the results.
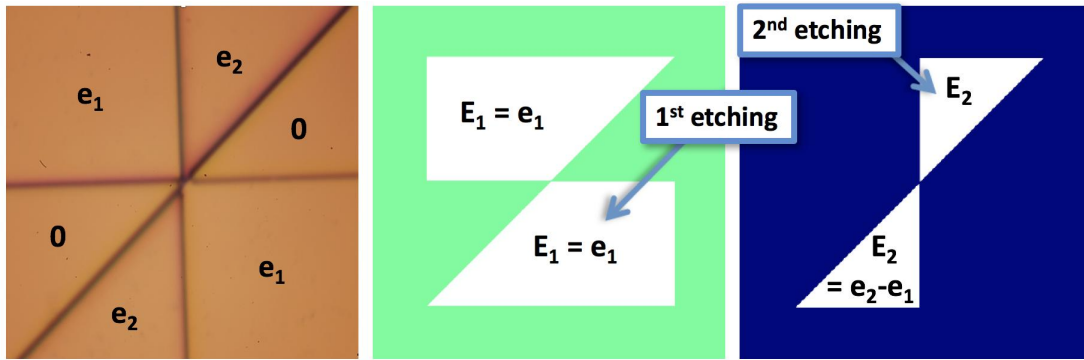
Figure 2. Image of the SLPM2 component obtained with a microscope (left) showing the six sectors with three different depths 0, e_1 or e_2. Etching process for manufacturing the SLPM, which is achieved in two sub-steps: a first etching (middle) of depth $E_1 = e_1$ everywhere except in two areas and a second etching (right) providing an additional depth $E_2 = e_2 - e_1$ in two other areas. As specified, $e_2 = 2e_1$ and $E_1 = E_2$.

2. THE SLPM COMPONENT

2.1 Design

The SLPM is made of one single piece of material, that is a thin silica glass with a thickness of about 1.5 mm in the visible wavelengths. It is split in six sectors with three different depths 0, e_1 and e_2 producing three levels of optical path difference and three uniform phase shifts of 0, π or 2π at the specified wavelength λ_0 (Fig. 1 and 2). The phase shifts ϕ_i are directly related to the sector depths e_i by: $\phi_i = 2\pi(n(\lambda) - 1) e_i/\lambda$, with $n(\lambda)$ the optical index of the SiO_2 material ($n = 1.453$ at 785 nm). For $\lambda =785$ nm, the sector depths should equal to $e_1 = 865$ nm and $e_2 = 1730$ nm. For $\lambda =700$ nm, it gives $e_1 = 772$ nm and $e_2 = 1544$ nm.

The SLPM is a sibling of the FQPM. While the FQPM is made of two etched quadrants (e_1 step) and two non-etched quadrants (no step), the SLPM is a centro-symmetric mask formed by two etched areas (e_1 step), two twice-etched areas (e_2 step) and two non-etched areas (no step). Ideally, $e_2 = 2e_1$ so that the SLPM induces at λ_0 a π-phase shift in two areas, a 2π-phase shift in two other areas and no phase shift elsewhere. Both FQPM and SLPM have two orthogonal transitions with a phase step of 0-π which provides a high on-axis attenuation. The SLPM is distinct from the FQPM with a new feature improving the achromatic behavior: a diagonal transition with a phase step of 0-2π. Using six sectors instead of four sectors enables to mitigate the chromatic effects of the SLPM compared to the FQPM while keeping the manufacturing easy.

Like for the FQPM, the main drawback of the SLPM is the horizontal and vertical transitions which strongly attenuate the signal of a putative exoplanet. The 0-2π transition transition is a new feature which is wavelength-dependent. While the 0-π transitions strongly constrain the detection limit at their position (in the 0, $\pi/2$, π and $3\pi/2$ angular directions), the 0-2π transitions slightly attenuate the transmission of a putative exoplanet flux (in the $\pi/4$ and $5\pi/4$ directions). This transmission may evolve with wavelength and a careful calibration of the instrument throughput will be required.

2.2 Manufacturing

The fabrication of the SLPM is based on UV lithography and is achieved in three basic steps. The six sector patterns are first defined by photolithography. The sector depths are then defined by lapping the uncoated sectors by reactive ion etching process, yielding to few nanometers of uncertainty for etching the depths. The process is achieved in two sub-steps (Fig. 2): a first etching of depth $E_1 = e_1$ everywhere except in two areas and a second etching providing an additional depth $E_2 = e_2 - e_1$ in two other areas. As specified, $e_2 = 2e_1$ and thus the two successive etchings should be equal to the specified etching depth $e_{spec} = E_1 = E_2$. However, a differential etching depths can be easily introduced during the etching process achieving an accuracy of $\pm$ 5 nm corresponding to about one degree in phase shift. The first limitation arises due to the lack of reproducibility of the etching depths E_1 and E_2 which are not equal and thus affect the sector depths $e_1 = E_1$ and $e_2 = E_1 + E_2$ in the component.
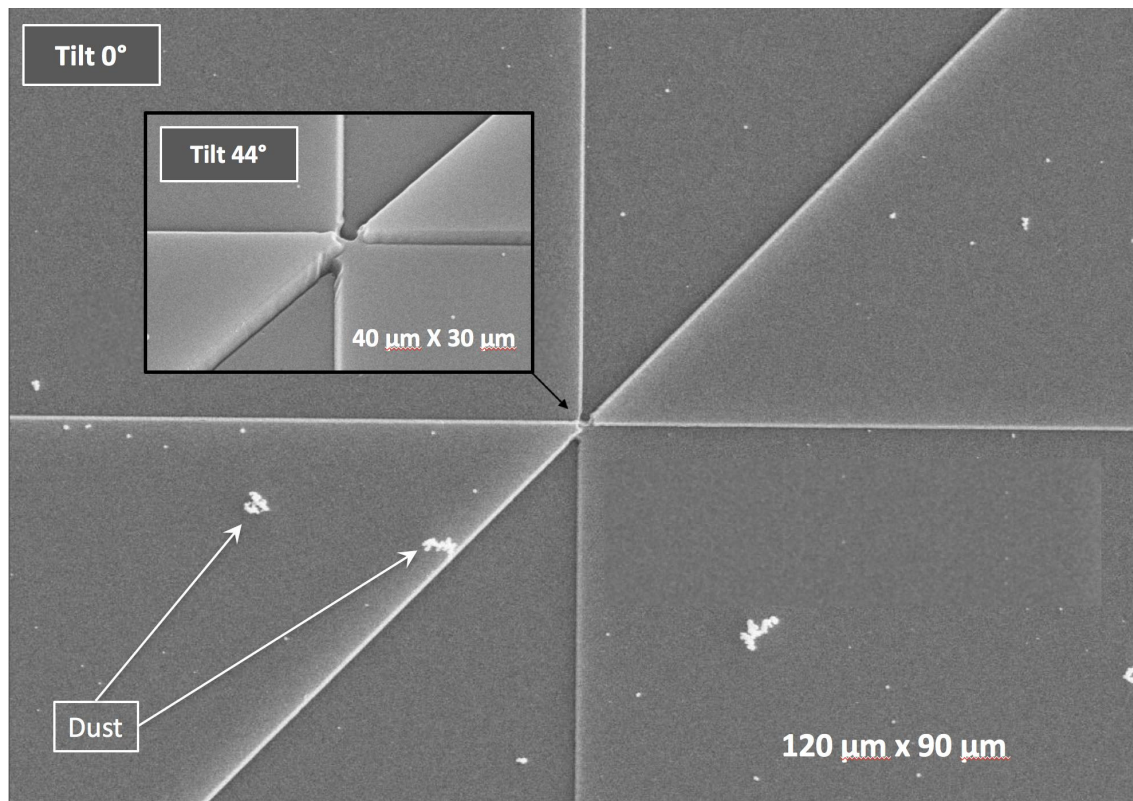
Figure 3. Images of the SLPM2 component obtained by a scanning electron microscope. The non-uniform illumination is due to the accumulation of electrons which occurs when sampling feature transitions.

The second limitation is due to the fact that the soft transitions between sectors are not steep but have a slope and thus a width. Such problem is inherent to the RIE (Reactive Ion Etching) process. A better definition of transitions can be reached using the deep etching DRIE (Deep Reactive Ion Etching) which is not available at GEPI. The slope prevents any transmission through the transition due to refraction and diffusion. To address this problem using the existing RIE process, we compensated the misalignment between the sector edges by setting proper offsets on the photolithography mask in order to align the middle of the slope of two opposite transitions (32). This likely allowed to diminish the refraction and diffusion issues and improve the coronagraph response.

2.3 Quality check

Two components SLPM2 and SLPM3 have been achieved and inspected with an optical microscope (Fig. 2) and a scanning electron microscope (Fig. 3 and 4) to highlight the defects introduced during the manufacturing. According to those images, the visual aspect of SLPM2 has a good quality. The global aspect is fine despite some dusts deposited onto the surface. In the central zone, there are 2 μm imperfections of the shape of the sectors extremities, but it is not critical since the Airy pattern falling onto the focal mask is significantly larger.

The transition aspects are fine. The transition widths w are rather thin, below 700 nm. We assume that the middle of the transition defines the sector edge and we deduce the misalignment between the sectors. The shift s between two parallel and opposite transitions is less than 300 nm for the horizontal, vertical and diagonal transitions. The misalignment between the three transitions passing onto the center is less than $s_0 \approx 500$ nm.

The sector depths e_1 and e_2 have been checked by using contact profilometry technique (Fig. 5) providing an accuracy of $\pm$ 10 nm. It shows that e_1 and e_2 are closed to the required specifications but departs from the specification by up to 15 nm (close to the transitions). The depth over the sector surface is relatively uniform despite a slope of about 3.5% on the e_2-depth sectors.
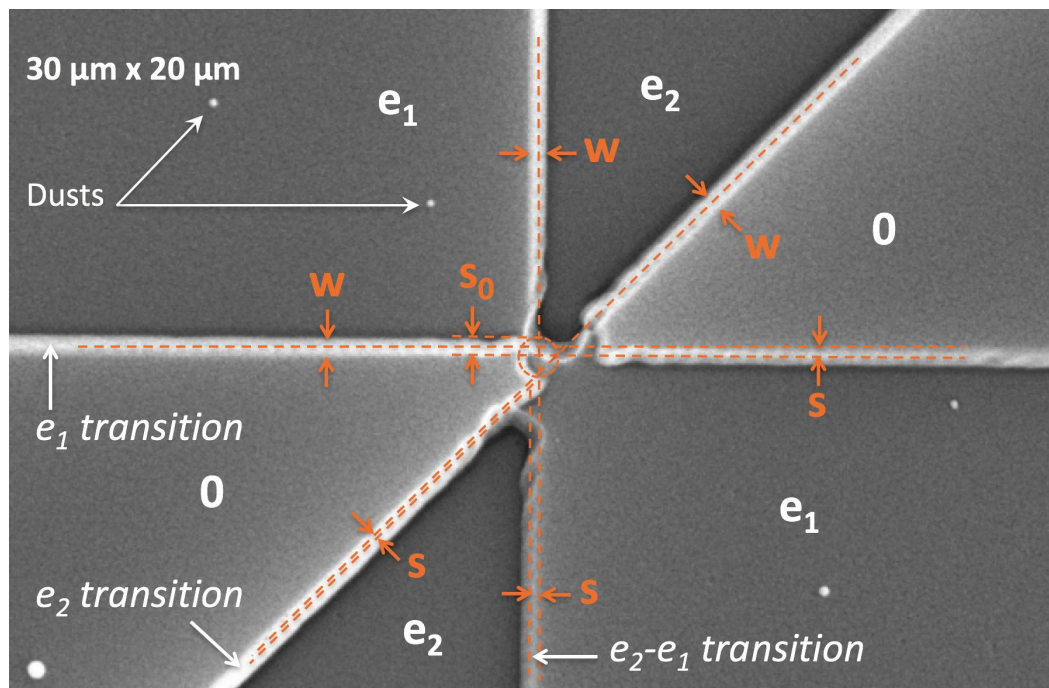
Figure 4. Image of the SLPM2 component obtained with a scanning electron microscope. The sector depths 0, e_1, e_2 and the transition steps e_1, e_2, $e_2 - e_1$ are labelled (in white). Manufacturing defects are highlighted (in orange): transition widths w, shift s between two parallel and opposite transitions, misalignment s_0 between the three transitions passing onto the center.
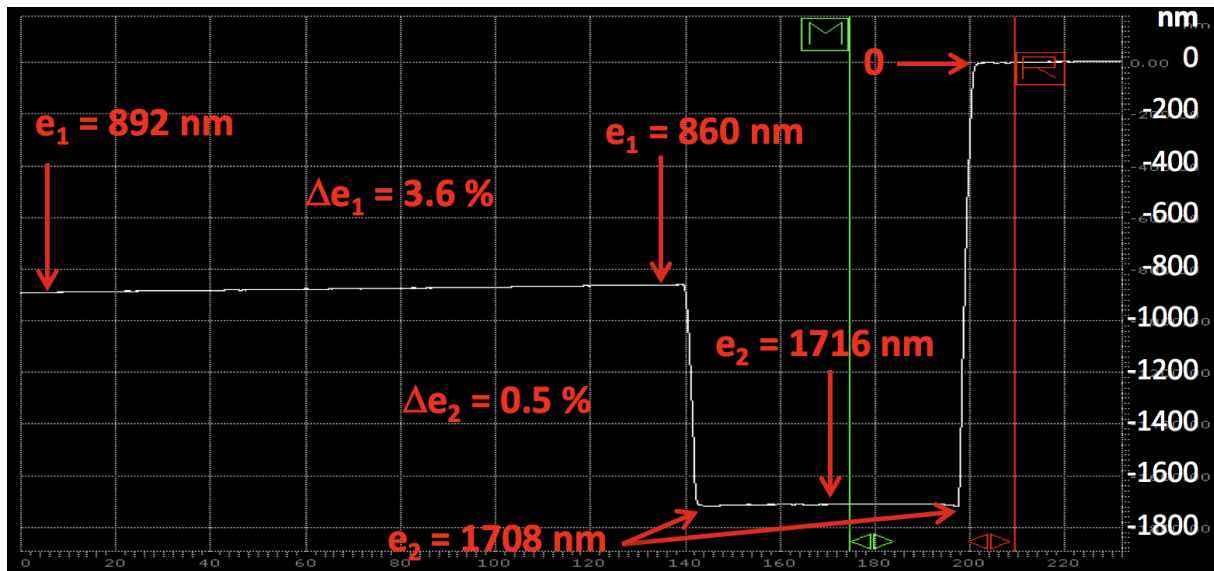

Figure 5. Sector depths of the SLPM2 measured by a contact profilometer providing an accuracy of $\pm$ 5nm. The measured transition steps are within the specifications at $\pm$ 15 nm.
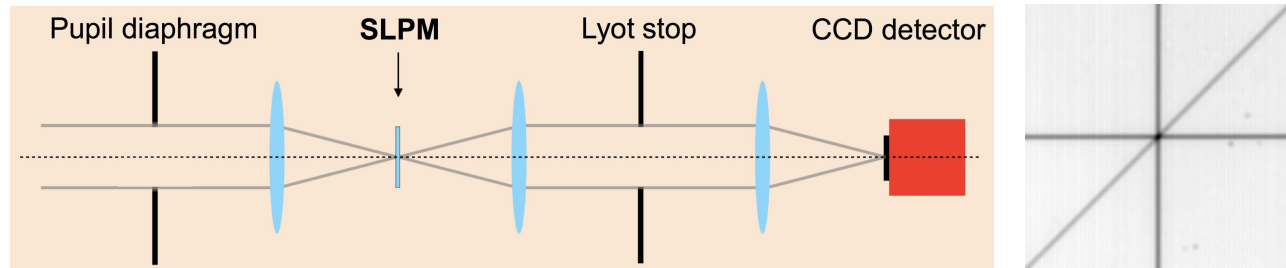
Figure 6. Optical scheme of the coronagraph (left): Diaphragm (in the entrance pupil plane), SLPM phase mask (in the focal plane), Lyot stop (in the relayed pupil plane), CCD detector (in the final focal plane). Flat illumination of the SLPM (right) obtained on the THD2 with an internal lamp which is used to align the CCD detector with the center of the image.

3. EXPERIMENTAL PROTOCOL

The THD2 bench (33; 34; 35; 36) was built to study and compare high-contrast imaging techniques with current/future ground-/space-based telescopes in the context of exoplanet science. The THD2 bench is compatible with many pupil plane or focal plane coronagraphs and allows reducing the starlight below a 10^{-8} contrast level in visible/near-infrared with narrow or broad bandwidth (37; 38). To reach such high performance, the THD2 bench includes :

- an chromatic design,
- a tip-tilt correction mirror associated to a low-order wavefront sensor (39),
- two deformable mirrors for compensating the residual aberrations both in phase and in amplitude,
- a focal-plane wavefront sensor that is the Self Coherent Camera (SCC) (37; 40; 41; 42),
- a fluxmeter and a spectrometer to measure in real time the injected light into the bench,
- an environment stabilization by means of three covers against dusts, thermal fluctuations and turbulence,
- a housekeeping (motorized alignements, 10 temperature/humidity sensors).

The light source is either a laser diode (640 nm, 700 nm or 785 nm) or a super continuum source plus 10-nm spectral filters (in the range 550-950 nm). The light is brought from the injection system of the source unit up to the bench by an optical fiber. The exit fiber head defines the first focal plane. A 8.1-mm circular diaphragm is placed in the first pupil plane. Before reaching the phase mask, the beam reflects on various optics including parabola and off-axis parabolae (OAP) as well as controlled mirrors: a tip-tilt mirror and two deformable mirrors. The light is then focused onto the focal phase mask. The beam is collimated by an OAP to go through the 6.5-mm Lyot stop in a pupil plane and is focused by another OAP onto the CCD detector (35).

We integrated the SLPM in the coronagraphic focal plane (Fig. 6). To avoid parasitic reflexion, the SLPM is tilted with respect to the incident angle by less than half a degree, producing negligible effects. An internal flat lamp provides a quasi-uniform illumination across the pupil and an image of the phase mask with its transitions (Fig. 6). After calibration of the TT-loop, we minimize the speckle intensity using the two deformable mirrors (35). Each deformable mirror has about 27 actuators across the pupil and about 22 actuators across the Lyot stop using the monochromatic laser diode centered at 700 nm.
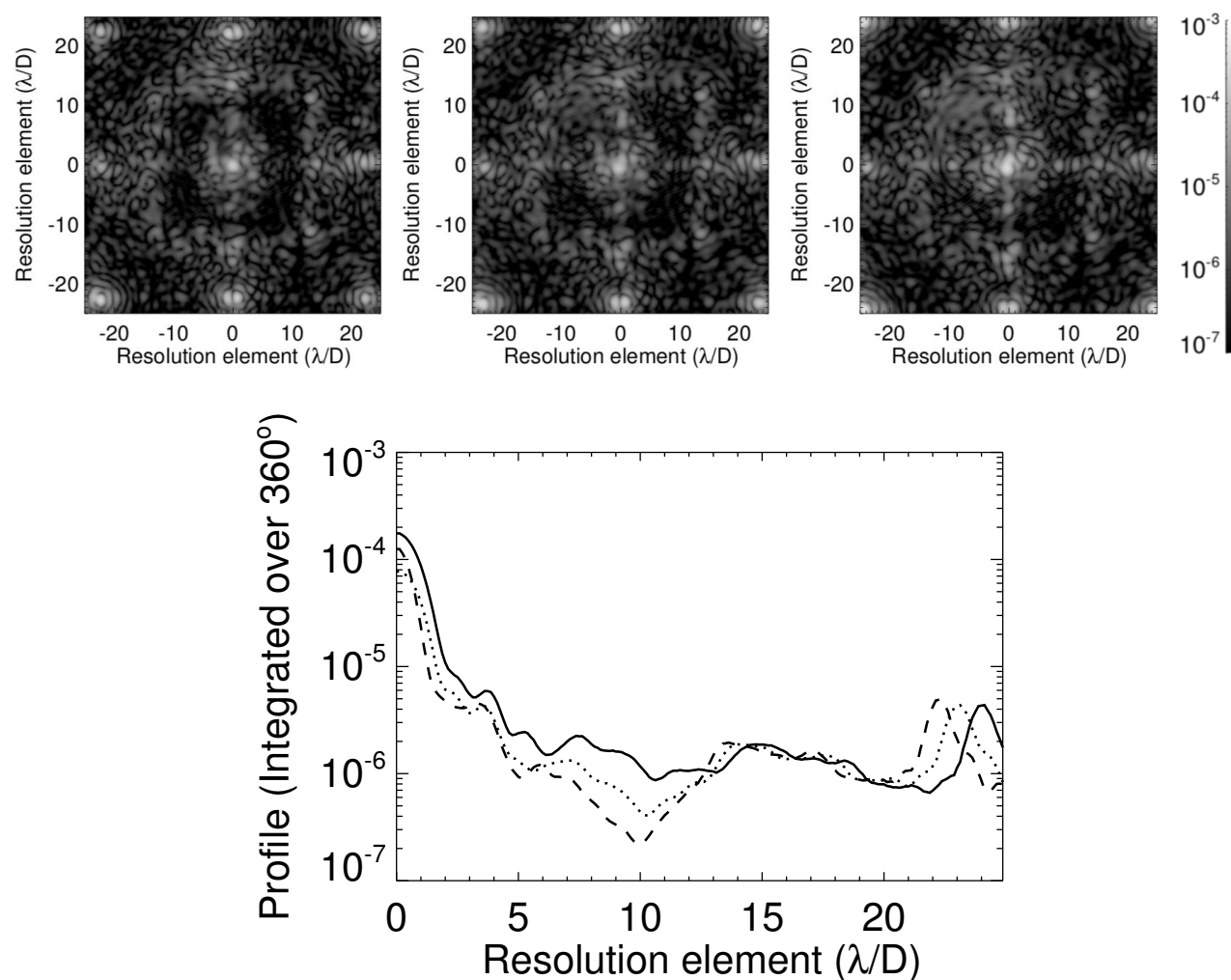
Figure 7. Coronagraphic images of SLPM3 over $50\,\lambda/D \times 50\,\lambda/D$ at 700 nm (left), 730 nm (middle), 760 nm (right). The profile is integrated over $360°$, including the transitions, at 700 nm (dashed line), 730 nm (dotted line), 760 nm (solid line). The dark area in which we minimize the speckle intensity has a radius of about 13.5 λ/D. The spatial scale is given in λ/D for $\lambda = 700$ nm so that the dark area is slightly larger than $13.5\,\lambda/D$ for 730 nm and 760 nm.
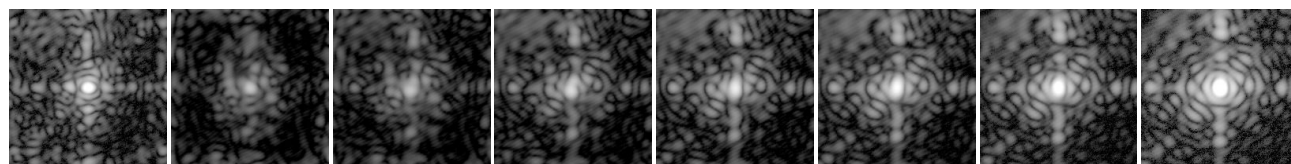

Figure 8. Coronagraphic images of SLPM3 zoomed onto the dark area over $25\,\lambda/D \times 25\,\lambda/D$. Left to right: 640 nm, 700 nm, 730 nm, 760 nm, 785 nm, 800 nm, 820 nm, 870 nm. Note that a "chromatic blurring" occurs at the top-left corner on the THD2 image, but it is mitigated at the central wavelength used for correction (700 nm).

4. EXPERIMENTAL RESULTS

Two components SLPM2 and SLPM3 have been tested onto the THD2 bench at LESIA. We record several coronagraphic images at different wavelengths in the range 550-950 nm (Fig. 7 and Fig. 8). Then, for each wavelength, we shift the beam at $\approx 5.7\lambda/D$ from the coronagraph center to record a point spread function (PSF). These PSFs are used to normalize the flux in the coronagraphic images. Thus, the flux normalization accounts for the SLPM transmission that is not 100%. Also, we account for the 65% transmission of the 6.5-mm Lyot stop (used with a 8.1mm entrance pupil). We record simultaneously data with a spectrometer and a fluxmeter to calibrate the wavelengths and the fluxes injected into the bench. The coronagraphic image is then normalized by the maximum of the off-axis PSFs (16).

Detection of a planet can be achieved down to 1 λ/D at small inner working angle ($\approx \lambda/D$) and large outer working angle ($\approx 13.5\lambda/D$ here). The SLPM enables wide-band high-contrast imaging. In Fig. 9, we plot the on-axis attenuation – the maximum of the -flux-normalized coronagraphic image – as a function of wavelength. The maximum on-axis attenuation reaches 2×10^{-5} for SLPM2 and 9×10^{-5} for SLPM3. It is better for SLPM2 by a factor of 4.5 compared to SLPM3. The on-axis attenuation over a 10% bandwidth remains better than 10^{-4} for SLPM2 and 3×10^{-4} for SLPM3. Along the diagonal transition, the off-axis transmission of SLPM2 is attenuated by less than 3% over a 10% bandwidth (16).

The optimal wavelength (corresponding to the maximum on-axis attenuation) occurs at ≈ 800 nm for SLPM2 and ≈ 715 nm for SLPM3, whereas the specified wavelength is 785 nm and 700 nm respectively. It yields in both cases to a wavelength shift of ≈ 15 nm. Note that the maximum on-axis attenuation for SLPM3 is estimated to 715 nm but it is comprised between 700 nm and 730 nm corresponding to the two lower data points. The on-axis attenuation is slightly better at 730 nm (15×10^{-5}) compared to the attenuation at 700 nm (9×10^{-5}), but the image at 700 nm contains less speckles than the image at 730 nm (Fig. 7).

5. NUMERICAL SIMULATIONS

We have performed numerical simulations to study how the SLPM behaves against manufacturing defects. We show (16) that the most critical specification is the depth e_2 which has to be exactly twice the depth e_1 (such as $e_2 = 2e_1$). Other transition defects (misalignment, width of transitions) are of second order and have been ignored in the numerical model. The theoretical model assumes perfect coronagraphs with perfect etchings and thicknesses, so that $e_1 = e_{spec}$ and $e_2 = 2e_{spec}$ with e_{spec} the specified etching depth at the specified wavelength $\lambda_{0,spec}$ which is the same for both successive etchings. The aberrated model is first optimized so as to fit the wings of the experimental data points which are far from the optimal wavelength. We choose $e_1 = e_2/2 = e_{spec} + \delta e$ where δe is a depth error assumed first to be equal for both successive etching steps. The aberrated model is then adjusted starting from the previous fit by fixing e_1 and by changing the value of e_2.

The model that minimizes the distance to the measurements (χ^2 minimization) is plotted in Fig. 10 for both device SLPM2 and SLPM3. In both cases, the model reproduces well the experimental data. The on-axis attenuation behave rather the same as a function of the wavelength. The maximum on-axis attenuation is affected for both components, while the optimal wavelength is shifted by $\delta\lambda \approx 15$ nm in the same direction to a higher wavelength. The design of SLPM2 was specified with an optimal wavelength $\lambda_{0,spec} = 785$ nm requiring depths of $e_1 = 865$ nm and $e_2 = 1730$ nm. However, the best experimental on-axis attenuation occurs at ≈ 800 nm. The best least squares fit of the experimental data corresponds to $e_1 = 866$ nm and $e_2 = 1726$ nm. For comparison, the SLPM3 was designed with $\lambda_{0,spec} = 700$ nm, $e_1 = 772$ nm and $e_2 = 1544$ nm. The maximum on-axis attenuation occurs at ≈ 715 nm and the best data fit yields to $e_1 = 789$ nm and $e_2 = 1564$ nm.

The main specification of the component is $e_2 = 2e_1$ but in practice the depth e_2 is not exactly twice the depth e_1. We define the depth errors introduced onto e_1 and e_2 as the difference between the specified and experimental values such as $\delta e_1 = e_1 - e_{spec}$ and $\delta e_2 = e_2 - 2e_{spec}$. The estimated sector depths depart from the theoretical value by less than 4 nm for SLPM2 and by up to 20 nm for SLPM3. We define also the differential depth error given by $\delta e_{12} = |e_2 - 2e_1|$ which quantify the departure from the main specification. SLPM2 performs better than SLPM3, their differential depth error $\delta e_{12} = |e_2 - 2e_1|$ being respectively equal to 6 nm (0.7%) and 14 nm (2%).
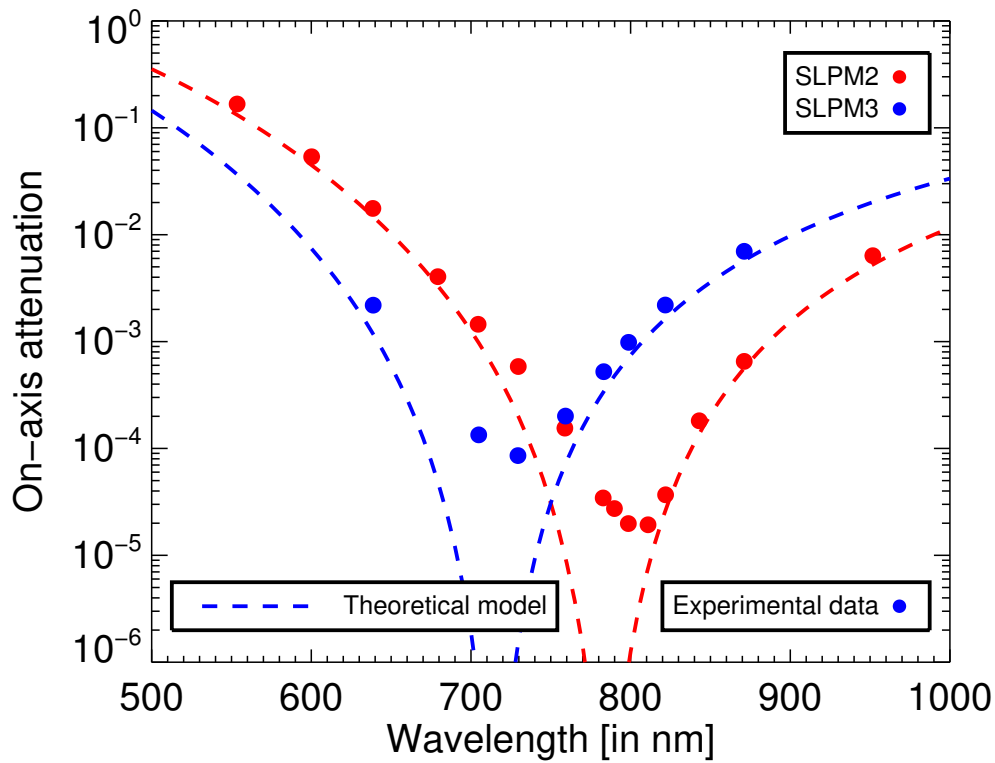
Figure 9. On-axis attenuation as a function of the wavelength. Comparison between SLPM2 (red) and SLPM3 (blue) for the theoretical model and the experimental data.
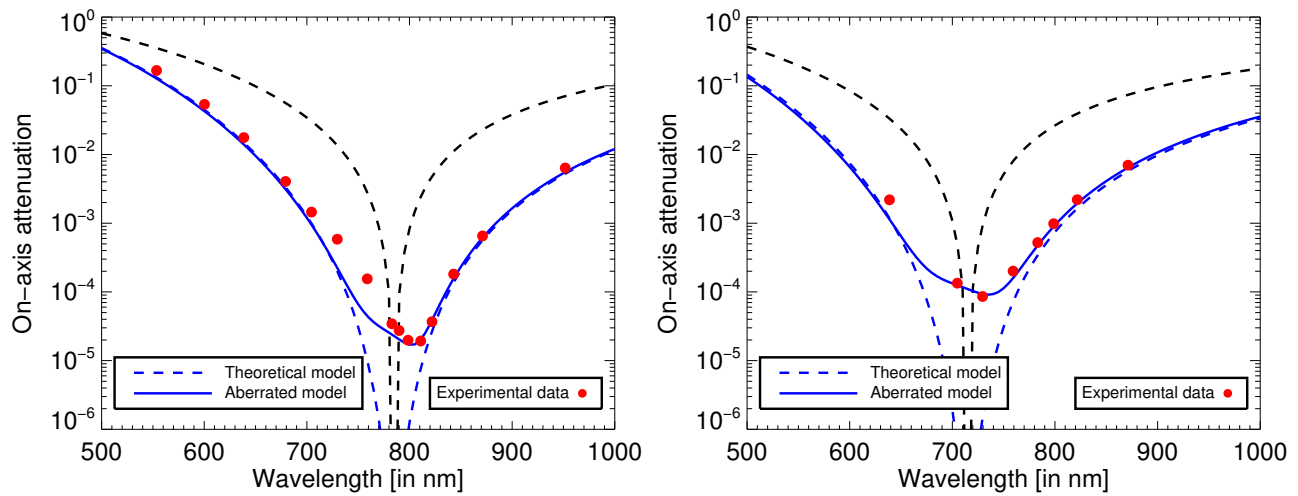

Figure 10. On-axis attenuation as a function of the wavelength of SLPM2 (left) and SLPM3 (right). Theoretical performance of the FQPM (dark dashed curve) and the SLPM (blue dashed curve) optimized at 785 nm (left) and 715 nm (right). Experimental data (red points). Simulated data (blue curve) for e1 = 789 nm and e2 = 1564 nm (left) or for e1 = 866 nm and e2 = 1726 nm (right).

The main manufacturing requirement is to ensure the same depths E_1 and E_2 for the two successive etchings. Knowing the sector depth errors obtained from the coronagraphic data, we deduce the etching depth errors occurring during the manufacturing. The first etching error $\delta E_1 = e_1 - e_{spec}$ equals to the sector depth error δe_1. The second etching equals to $e_2 - e_1$ so that its error equals to $\delta E_2 = e_2 - e_1 - e_{spec}$. For SLPM2, the two etching depth errors are rather small, ranging from 1 nm (0.1%) to 5 nm (0.6%). For SLPM3, the first etching depth error of 17 nm (2.2%) is significantly higher than the second one of 3 nm (0.4%). The reason why SLPM3 is less efficient than SLPM2 is thus due to larger etching depth errors.

To resume, the main parameters and performance of SLPM2 and SLPM3 are given in table 1.

Parameters	Symbols	**SLPM2**	**SLPM3**
Maximum on-axis attenuation	τ_{max}	$\approx 2 \times 10^{-5}$	$\approx 9 \times 10^{-5}$
Attenuation over 10% bandwidth	$\tau_{10\%}$	$< 1 \times 10^{-4}$	$< 3 \times 10^{-4}$
Specified wavelength	$\lambda_{0,spec}$	$= 785$ nm	$= 700$ nm
Optimal wavelength (for τ_{max})	λ_0	≈ 800 nm	≈ 715 nm
Optimal wavelength shift	$\delta\lambda$	≈ 15 nm (1.9%)	≈ 15 nm (2.1%)
Specified depth 1	e_{spec}	$= 865$ nm	$= 772$ nm
Estimated depth 1	e_1	≈ 866 nm	≈ 789 nm
Error on depth 1	$\delta e_1 = e_1 - e_{spec}$	$\approx +1$ nm (0.1%)	$\approx +17$ nm (2.2%)
Corresponding wavelength 1	λ_1	≈ 785 nm	≈ 715 nm
Specified depth 2	$2e_{spec}$	$= 1730$ nm	$= 1544$ nm
Estimated depth 2	e_2	≈ 1726 nm	≈ 1564 nm
Error on depth 2	$\delta e_2 = e_2 - 2e_{spec}$	$\approx$ -4 nm (0.2%)	$\approx +20$ nm (1.3%)
Corresponding wavelength 2	λ_2	≈ 782.5 nm	≈ 710 nm
Differential depth error	$\delta e_{12} = |e_2 - 2e_1|$	≈ 6 nm (0.7%)	≈ 14 nm (2%)
Estimated depth of the first etching	$E_1 = e_1$	≈ 866 nm	≈ 789 nm
Error on the first etching	$\delta E_1 = e_1 - e_{spec}$	$\approx +1$ nm (0.1%)	$\approx +17$ nm (2.2%)
Estimated depth of the second etching	$E_2 = e_2 - e_1$	≈ 860 nm	≈ 775 nm
Error on the second etching	$\delta E_2 = e_2 - e_1 - e_{spec}$	$\approx$ -5 nm (0.6%)	$\approx +3$ nm (0.4%)

Table 1. Specified and estimated parameters as well as experimental performance of SLPM2 and SLPM3.

6. CONCLUSION

A collaboration between GEPI and LESIA laboratories at Paris Observatory has been initiated for producing SLPM components that were proposed by the Shanghai University team. We tested two SLPMs components at visible wavelengths onto the THD2 bench. The SLPM components manufactured at GEPI enable wide-band high-contrast imaging. They reaches an on-axis attenuation of the order of 10^{-4} to 10^{-5} down to 1 λ/D on 10% bandwidth. Thus, the SLPM is easy to fabricate at low cost and easy to implement with a unique focal plane mask and no need of pupil apodization.

However, any etching imperfections can affect the SLPM performance, by lowering the on-axis attenuation onto the optical axis at wavelengths close to the optimal one and by changing the optimal wavelength where the maximum on-axis attenuation occurs (16). Despite few nanometers of uncertainty for etching the depths, we show that these first components performs efficiently. SLPM2 performs better than SLPM3 by providing a higher attenuation (by a factor of 4.5). Their differential depth error are equal to 6 nm (0.7%) for SLPM2 and 14 nm (2%) for SLPM3. This is due to larger etching depth errors introduced during the manufacturing (up to 17 nm for SLPM3 and up to 5 nm only for SLPM2).

An accuracy better than $\pm$ 1 nm for etching the depths is required for providing an on-axis attenuation deeper than 10^{-5}, knowing that it should be in principle infinite at the optimal wavelength. However, the accuracy for etching the phase mask by photolithography is currently limited to $\pm$ 5 nm at GEPI. A solution should be to etch one depth only, to measure it by profilometry before etching the second depth in order to try to equalize both etching depths. Other manufacturing processes may reach the 1-nm requirement but at a higher cost.

ACKNOWLEDGMENTS

References

[1] Guyon, O., Pluzhnik, E. A., Kuchner, M. J., Collins, B., and Ridgway, S. T., "Theoretical Limits on Extrasolar Terrestrial Planet Detection with Coronagraphs," *Astrophysical Journal, Supplement* **167**, 81–99 (Nov. 2006).

[2] Mawet, D., Pueyo, L., Lawson, P., Mugnier, L., Traub, W., Boccaletti, A., Trauger, J. T., Gladysz, S., Serabyn, E., Milli, J., Belikov, R., Kasper, M., Baudoz, P., Macintosh, B., Marois, C., Oppenheimer, B., Barrett, H., Beuzit, J.-L., Devaney, N., Girard, J., Guyon, O., Krist, J., Mennesson, B., Mouillet, D., Murakami, N., Poyneer, L., Savransky, D., Vérinaud, C., and Wallace, J. K., "Review of small-angle coronagraphic techniques in the wake of ground-based second-generation adaptive optics systems," in [*Space Telescopes and Instrumentation 2012: Optical, Infrared, and Millimeter Wave*], *Proc. SPIE* **8442**, 844204 (Sept. 2012).

[3] Lyot, B., "The study of the solar corona and prominences without eclipses (George Darwin Lecture, 1939)," *Monthly Notices of the Royal Astronomical Society* **99**, 580 (June 1939).

[4] Roddier, F. and Roddier, C., "Stellar Coronograph with Phase Mask," *Publications of the ASP* **109**, 815–820 (July 1997).

[5] N'diaye, M., Dohlen, K., Cuevas, S., Lanzoni, P., Chemla, F., Chaumont, C., Soummer, R., and Griffiths, E. T., "Experimental results with a second-generation Roddier & Roddier phase mask coronagraph," *Astronomy and Astrophysics* **509**, A8 (Jan. 2010).

[6] Abe, L., Vakili, F., and Boccaletti, A., "The achromatic phase knife coronagraph," *Astronomy and Astrophysics* **374**, 1161–1168 (Aug. 2001).

[7] Abe, L., Domiciano de Souza, Jr., A., Vakili, F., and Gay, J., "Phase Knife Coronagraph. II - Laboratory results," *Astronomy and Astrophysics* **400**, 385–392 (Mar. 2003).

[8] Soummer, R., Dohlen, K., and Aime, C., "Achromatic dual-zone phase mask stellar coronagraph," *Astronomy and Astrophysics* **403**, 369–381 (May 2003).

[9] Rouan, D., Riaud, P., Boccaletti, A., Clénet, Y., and Labeyrie, A., "The Four-Quadrant Phase-Mask Coronagraph. I. Principle," *Publications of the ASP* **112**, 1479–1486 (Nov. 2000).

[10] Riaud, P., Boccaletti, A., Rouan, D., Lemarquis, F., and Labeyrie, A., "The Four-Quadrant Phase-Mask Coronagraph. II. Simulations," *Publications of the ASP* **113**, 1145–1154 (Sept. 2001).

[11] Riaud, P., Boccaletti, A., Baudrand, J., and Rouan, D., "The Four-Quadrant Phase Mask Coronagraph. III. Laboratory Performance," *Publications of the ASP* **115**, 712–719 (June 2003).

[12] Boccaletti, A., Riaud, P., Baudoz, P., Baudrand, J., Rouan, D., Gratadour, D., Lacombe, F., and Lagrange, A.-M., "The Four-Quadrant Phase Mask Coronagraph. IV. First Light at the Very Large Telescope," *Publications of the ASP* **116**, 1061–1071 (Nov. 2004).

[13] Baudoz, P., Boccaletti, A., Riaud, P., Cavarroc, C., Baudrand, J., Reess, J. M., and Rouan, D., "Feasibility of the Four-Quadrant Phase Mask in the Mid-Infrared on the James Webb Space Telescope," *Publications of the ASP* **118**, 765–773 (May 2006).

[14] Ma, O., Cao, Q., and Hou, F., "Wide-band coronagraph with sinusoidal phase in the angular direction," *Optics Express* **20**, 10933 (May 2012).

[15] Hou, F., Cao, Q., Zhu, M., and Ma, O., "Wide-band six-region phase mask coronagraph," *Optics Express* **22**, 1884 (Jan. 2014).

[16] Patru, F., Baudoz, P., Galicher, R., Cao, Q., Wang, K., Xing, L., Boussaha, F., Firminy, J., and Bonafous, M., "Laboratory demonstration of a broadband six-level phase mask coronagraph," *Optics Express* **26**, 10007 (Apr. 2018).

[17] Murakami, N., Uemura, R., Baba, N., Nishikawa, J., Tamura, M., Hashimoto, N., and Abe, L., "An Eight-Octant Phase-Mask Coronagraph," *Publications of the ASP* **120**, 1112 (Oct. 2008).

[18] Mawet, D., Riaud, P., Absil, O., and Surdej, J., "Annular Groove Phase Mask Coronagraph," *Astrophysical Journal* **633**, 1191–1200 (Nov. 2005).

[19] Foo, G., Palacios, D. M., and Swartzlander, Jr., G. A., "Optical vortex coronagraph," *Optics Letters* **30**, 3308–3310 (Dec. 2005).

[20] Mawet, D., Riaud, P., Baudrand, J., Baudoz, P., Boccaletti, A., Dupuis, O., and Rouan, D., "The four-quadrant phase-mask coronagraph: white light laboratory results with an achromatic device," *Astronomy and Astrophysics* **448**, 801–808 (Mar. 2006).

[21] Mawet, D., Riaud, P., Hanot, C., Vandormael, D., Loicq, J., Baudrand, J., Surdej, J., and Habraken, S., "The annular groove phase mask coronagraph: an achromatic optical vortex," in [*Techniques and Instrumentation for Detection of Exoplanets III*], *Proc. SPIE* **6693**, 66931M (Sept. 2007).

[22] Carlotti, A., Aime, C., and Ricort, G., "Phase mask coronagraphy: use of a Mach-Zehnder interferometer for achromatic four-quadrant phase masks," in [*Optical and Infrared Interferometry*], *Proc. SPIE* **7013**, 70133S (July 2008).

[23] Murakami, N., Nishikawa, J., Yokochi, K., Tamura, M., Baba, N., and Abe, L., "Achromatic Eight-octant Phase-mask Coronagraph using Photonic Crystal," *Astrophysical Journal* **714**, 772–777 (May 2010).

[24] Soummer, R., Sivaramakrishnan, A., Pueyo, L., Macintosh, B., and Oppenheimer, B. R., "Apodized Pupil Lyot Coronagraphs for Arbitrary Apertures. III. Quasi-achromatic Solutions," *Astrophysical Journal* **729**, 144 (Mar. 2011).

[25] N'diaye, M., Dohlen, K., Cuevas, S., Soummer, R., Sánchez-Pérez, C., and Zamkotsian, F., "Improved achromatization of phase mask coronagraphs using colored apodization," *Astronomy and Astrophysics* **538**, A55 (Feb. 2012).

[26] Errmann, R., Minardi, S., and Pertsch, T., "A broad-band scalar vortex coronagraph," *Monthly Notices of the Royal Astronomical Society* **435**, 565–569 (Oct. 2013).

[27] Newman, K., Guyon, O., Balasubramanian, K., Belikov, R., Jovanovic, N., Martinache, F., and Wilson, D., "An Achromatic Focal Plane Mask for High-Performance Broadband Coronagraphy," *Publications of the ASP* **127**, 437 (May 2015).

[28] Galicher, R., Baudoz, P., and Baudrand, J., "Multi-stage four-quadrant phase mask: achromatic coronagraph for space-based and ground-based telescopes," *Astronomy and Astrophysics* **530**, A43 (June 2011).

[29] Ge, Y., Cao, Q., Hu, R., Wang, K., and Tong, X., "Cascade six-level phase-mask achromatic coronagraph," *Applied Optics* **55**, 1006 (Feb. 2016).

[30] Mawet, D., Serabyn, E., Wallace, J. K., and Pueyo, L., "Improved high-contrast imaging with on-axis telescopes using a multistage vortex coronagraph," *Optics Letters* **36**, 1506 (Apr. 2011).

[31] Mawet, D., Murakami, N., Delacroix, C., Serabyn, E., Absil, O., Baba, N., Baudrand, J., Boccaletti, A., Burruss, R., Chipman, R., Forsberg, P., Habraken, S., Hamaguchi, S., Hanot, C., Ise, A., Karlsson, M., Kern, B., Krist, J., Kuhnert, A., Levine, M., Liewer, K., McClain, S., McEldowney, S., Mennesson, B., Moody, D., Murakami, H., Niessner, A., Nishikawa, J., O'Brien, N., Oka, K., Park, P., Piron, P., Pueyo, L., Riaud, P., Sakamoto, M., Tamura, M., Trauger, J., Shemo, D., Surdej, J., Tabirian, N., Traub, W., Wallace, J., and Yokochi, K., "Taking the vector vortex coronagraph to the next level for ground- and space-based exoplanet imaging instruments: review of technology developments in the USA, Japan, and Europe," in [*Techniques and Instrumentation for Detection of Exoplanets V*], *Proc. SPIE* **8151**, 815108 (Oct. 2011).

[32] Bonafous, M., Galicher, R., Baudoz, P., Firminy, J., and Boussaha, F., "Development and characterization of Four-Quadrant Phase Mask coronagraph (FQPM)," in [*Advances in Optical and Mechanical Technologies for Telescopes and Instrumentation II*], *Proc. SPIE* **9912**, 99126J (July 2016).

[33] Galicher, R., Baudoz, P., Delorme, J. R., Mazoyer, J., Rousset, G., Firminy, J., Boussaha, F., N'Diaye, M., Dohlen, K., and Caillat, A., "High contrast imaging on the THD bench: progress and upgrades," in [*Space Telescopes and Instrumentation 2014: Optical, Infrared, and Millimeter Wave*], *Proc. SPIE* **9143**, 91435A (Aug. 2014).

[34] Baudoz, P., Galicher, R., Patru, F., Dupuis, O., and S., T., "Status and performance of the THD2 bench in multi-deformable mirror configuration," *Adaptive Optics for Extremely Large Telescopes conf* **5** (2017).

[35] Baudoz, P., Potier, A., Galicher, R., and Patru, F., "The THD2 bench," *Proc. SPIE* **, this proceeding** (June 2018).

[36] Potier, A., Baudoz, P., and Galicher, R., "High contrast imaging test bench to its limits: the THD2 bench," *Proc. SPIE* **, this proceeding** (June 2018).

[37] Mazoyer, J., Baudoz, P., Galicher, R., and Rousset, G., "High-contrast imaging in polychromatic light with the self-coherent camera," *Astronomy and Astrophysics* **564**, L1 (Apr. 2014).

[38] Delorme, J. R., N'Diaye, M., Galicher, R., Dohlen, K., Baudoz, P., Caillat, A., Rousset, G., Soummer, R., and Dupuis, O., "Laboratory validation of the dual-zone phase mask coronagraph in broadband light at the high-contrast imaging THD testbed," *Astronomy and Astrophysics* **592**, A119 (Aug. 2016).

[39] Singh, G., Martinache, F., Baudoz, P., Guyon, O., Matsuo, T., Jovanovic, N., and Clergeon, C., "Lyot-based Low Order Wavefront Sensor for Phase-mask Coronagraphs: Principle, Simulations and Laboratory Experiments," *Publications of the ASP* **126**, 586 (June 2014).

[40] Galicher, R., Baudoz, P., and Rousset, G., "Wavefront error correction and Earth-like planet detection by a self-coherent camera in space," *Astronomy and Astrophysics* **488**, L9–L12 (Sept. 2008).

[41] Galicher, R., Baudoz, P., Rousset, G., Totems, J., and Mas, M., "Self-coherent camera as a focal plane wavefront sensor: simulations," *Astronomy and Astrophysics* **509**, A31 (Jan. 2010).

[42] Mazoyer, J., Baudoz, P., Galicher, R., Mas, M., and Rousset, G., "Estimation and correction of wavefront aberrations using the self-coherent camera: laboratory results," *Astronomy and Astrophysics* **557**, A9 (Sept. 2013).